

1 **Structure and radiation response of anion excess bixbyite**



3 Maulik Patel

4 *The University of Liverpool, School of Engineering,*  
5 *Department of Mechanical, Materials and Aerospace Engineering,*  
6 *Liverpool, L69 3GH, United Kingdom\**

7 Jeffery Aguiar

8 *The University of Utah, 301 presidents circle, Salt Lake City, Utah 84109, USA<sup>†</sup>*

9 Kurt Sickafus

10 *Los Alamos National Laboratory, Materials Science and Technology Division,*  
11 *Los Alamos, New Mexico 87545, USA<sup>‡</sup> and*  
12 *The University of Tennessee, Department of Materials*  
13 *Science and Engineering, Knoxville, TN 37996, USA*

14 Gianguido Baldinozzi

15 *Université Paris–Saclay, CentraleSupélec, CNRS, Structures,*  
16 *Propriétés et Modélisation des Solides, 91190 Gif-sur-Yvette, France<sup>§</sup>*

17 (Dated: November 20, 2021)

## Abstract

The crystal structure analysis of  $\text{Gd}_2\text{Ce}_2\text{O}_7$  reveals that it crystallizes in a bixbyite-type symmetry ( $I2_13$ ) heretofore never reported among the known fluorite derivative compounds. Analysis of the structure suggests a randomly occupied cation sub-lattice with infinite correlation length associated with long-range ordered anion sub-lattice with half of the vacant sites of an ideal bixbyite filled, hence the name 'anion-excess bixbyite'. Ion irradiation experiments and quantitative x-ray diffraction analysis were used to study the separate response of the anion sub-lattice to swift heavy ion radiation. Analysis of anion and cation correlation lengths as a function of fluence shows that the topological disorder on the anion sub-lattice grows faster than that on the cation sub-lattice. The microstructural response at increasing radiation fluences leads to a decrease of the strain after an initial increase while the variance of the strain increases following the increase of the microdomain wall density. This particular behaviour seems responsible for the exceptional radiation resistance of this system that does not display any significant amorphisation, even at the highest fluence.

---

\* maulik@liverpool.ac.uk

† Jeffery.Aguiar@gmail.com

‡ kurt@lanl.gov

§ gianguido.baldinozzi@centralesupelec.fr

## 18 I. INTRODUCTION

19 The family of oxygen deficient fluorite compounds has gained significant interest as sys-  
20 tems for minor actinides disposal and understanding spent fuel chemistry, though they can  
21 be interesting systems also for their magnetic properties, their low thermal conductivity,  
22 and as ionic conductors [1–6]. Apart from these technological interests, these oxides provide  
23 a fascinating playground to explore the order mechanisms arising from flexible aliovalent  
24 doping and non-stoichiometry [7–15]. In most of these compounds, the preferred mechanism  
25 of charge compensation of the aliovalent doping is the creation of O vacancies. In some  
26 of these compounds, cation and anion vacancies do order long-range (eg. pyrochlores and  
27 weberites), while in other ones, only the oxygen vacancies order (as for instance the  $\beta, \gamma,$   
28 and  $\delta$  phases [16–18] in the mixed oxides of scandium with zirconium or hafnium). In other  
29 compounds, neither cations nor anions exhibit a long-range site selectivity (as for instance  
30  $\text{Y}_2\text{Zr}_2\text{O}_7$ ). These characteristics are particularly interesting because they may facilitate the  
31 separation of the specific response of the cation and anion sub-lattices to radiation damage.  
32 While structural changes induced by irradiation have been extensively studied in the sys-  
33 tems where cations are initially ordered [19–23] and in systems where both sub-lattices do  
34 not display long-range order, the irradiation behavior of fluorite-related oxide systems where  
35 the cations are randomly distributed but the anions are highly ordered is not quantitatively  
36 explored yet. This is partly due to the relative rarity of such model systems. The search for  
37 such a system has lead us to take a closer look at the phases formed in the  $\text{CeO}_2\text{--Gd}_2\text{O}_3$   
38 pseudo-binary system. In this system, while a single phase of fluorite structure oxide is ob-  
39 served in the Ce-rich region, a C-type phase is encountered in the Gd-rich region. This is also  
40 generally true for other  $\text{CeO}_2\text{--Ln}_2\text{O}_3$  systems (where Ln is a lanthanide element) [9]. Among  
41 this class of compounds, with compositions close to a morphotropic boundary,  $\text{Gd}_2\text{Ce}_2\text{O}_7$   
42 was previously reported to crystallize with a structure related to a bixbyite phase [24, 25].  
43 In this compound, the statistically weighted mean cation radius,  $\langle r_M \rangle$  is large enough to  
44 favour the 8-fold coordination of the cation typical of a fluorite phase against the possible  
45 structural polymorphism driven by the preference for an octahedral environment typical of  
46 a smaller-size cation. But this is not the only specific feature of this compound.

47 When a mixture of cations shares a single crystallographic site, the determination of short-  
48 range properties related to the exact cation distribution is a complex task that requires a

49 precise analysis of the diffuse scattering. Nevertheless, long-wavelength collective properties  
50 (elastic properties, ...) that can promote the vacancy ordering might not be extremely  
51 sensitive to these short-range details. When the compositional fluctuations are small to a  
52 scale much larger than the lattice spacing, it can be possible to coarse-grain the material  
53 composition and describe the site occupancy using a scalar composition field that is the  
54 average of the elemental site occupancies over several cells. The price we pay with this  
55 formalism is that we lose the contribution of the short-range fluctuations to the entropy. In  
56 this respect,  $\text{Gd}_2\text{Ce}_2\text{O}_7$  is particularly interesting because not only the weighted mean cation  
57 radius has an optimum value for the fluorite structure, but also the size mismatch between  
58 the two cation vanishes. This size mismatch is better defined by the statistical variance of  
59 the distribution of the radii, ( $\sigma^2 = \langle r_M^2 \rangle - \langle r_M \rangle^2$ , **that is the second central moment of**  
60 **the radii distribution** [26]). Indeed, a mismatch can promote effectively cation order and  
61 also favour cation off-site displacements from their ideal fluorite positions. Also, it can  
62 help in stabilising long-range cooperative displacements that can actively interfere with the  
63 ordering of the O vacancies. This effect is minimal or even absent in  $\text{Gd}_2\text{Ce}_2\text{O}_7$ , therefore,  
64 in this system the cations have a neutral or minimal influence on the long-range order in the  
65 anion sub-lattice leading to a decoupled behaviour for the characteristic patterns of the O  
66 vacancies.

67 This characteristic property of  $\text{Gd}_2\text{Ce}_2\text{O}_7$  is particularly interesting because it allows to  
68 study the specific response of the anion sub-lattice to radiation damage. In this manuscript,  
69 (1) we present a careful analysis of the characteristic of the O vacancy order in the pristine  
70 structure of  $\text{Gd}_2\text{Ce}_2\text{O}_7$  whose hallmark is the long-range order of the anions decoupled from  
71 any significant site selectivity of the cations; and (2) we follow the radiation response of the  
72 anion sub-lattice where the significant mobility of the O vacancies just above room tem-  
73 perature provides an efficient mechanism for healing the radiation damage occurring in this  
74 system. Indeed, this fluorite-related system does not display any significant amorphisation  
75 even at the highest fluences of the swift heavy ion irradiation experiment.

## 76 II. EXPERIMENTAL PROCEDURES

77 Powders of cerium dioxide ( $\text{CeO}_2$ , 99.99%) and gadolinium sesquioxide ( $\text{Gd}_2\text{O}_3$ , 99.99%)  
78 purchased from Alfa Aesar were calcined at 700°C and weighed to obtain a 2:2:7 stoichiomet-

79 ric ratio of Gd:Ce:O. These mixtures were ground in isopropanol medium in a large Agate  
80 mortar for 12 hours. The powder mixture was cold pressed into disks of 8 mm diameter  
81 and 1 mm thickness using a tungsten carbide die and plunger. The disks were then sintered  
82 twice in air, first at 1200°C for 24 hours and then at 1400°C for 48 hours with the heating  
83 and cooling rates of 2°C/min and with intermittent regrinding between the two sintering  
84 cycles.

85 To study the radiation response of  $\text{Gd}_2\text{Ce}_2\text{O}_7$ , discs of 8mm diameter and 2 mm thickness  
86 were irradiated at room temperature by 92 MeV  $\text{Xe}^{26+}$  ions at IRRSUD facility at GANIL,  
87 France, using fluences ranging from  $10^{11}$  to  $10^{14}$  ions/cm<sup>2</sup>. The flux of ions during irradiation  
88 was  $10^9$  ions/cm<sup>2</sup>/s and the sample surface was kept normal to the ion beam direction. X-ray  
89 diffraction (XRD) measurements were performed only on samples irradiated with fluences  
90 above  $10^{12}$  ions/cm<sup>2</sup>, that correspond to the conditions of a uniformly irradiated surface  
91 due to multiple track overlaps. The range and stopping powers of 92 MeV  $\text{Xe}^{26+}$  ions in  
92  $\text{Gd}_2\text{Ce}_2\text{O}_7$  was estimated using Monte-Carlo simulation program SRIM [27]. The plot of  
93 nuclear and electronic energy loss v/s depth shows that these ions lose energy primarily in  
94 the electronic stopping regime (Figure 1a).

95 The projected range of these ions in  $\text{Gd}_2\text{Ce}_2\text{O}_7$  is 9  $\mu\text{m}$  while the penetration depth of  
96 Cu  $\text{K}\alpha$  x-rays used for the XRD experiments is always less than 2.5  $\mu\text{m}$ , even at high angles  
97  $\theta$  formed by the impinging X-ray beam and the sample surface (Figure 1b). Hence, XRD  
98 can be carried out in a bisecting reflection geometry to assess the structural modifications  
99 in the pristine and in the damaged layer of the irradiated samples. The implanted layer and  
100 the pristine layer in the irradiated pellets do not contribute to the intensity of the scattered  
101 beam.

102 X-ray powder diffraction experiments were performed to characterise the structure of  
103 the as-synthesised samples and the pellets used for the irradiation experiment. XRD was  
104 performed using a Bruker D8 Advance diffractometer equipped with a Göbel mirror for Cu  
105  $\text{K}\alpha$  radiation and a NaI scintillation detector. For reasons mentioned above, data collection  
106 was performed in a  $\theta-\theta$  geometry performing symmetric step scans of the detector and X-ray  
107 source ( $\Delta 2\theta = 0.02^\circ$ , and  $2\theta$  range 10-80°) and a step time of 2 sec/step. Rietveld refinements  
108 were performed using the software Xnd [28]. The parameters defining the instrumental  
109 broadening (transfer function) of the diffractometer were determined using a LaB<sub>6</sub> NIST-  
110 660C standard sample stored in Argon.

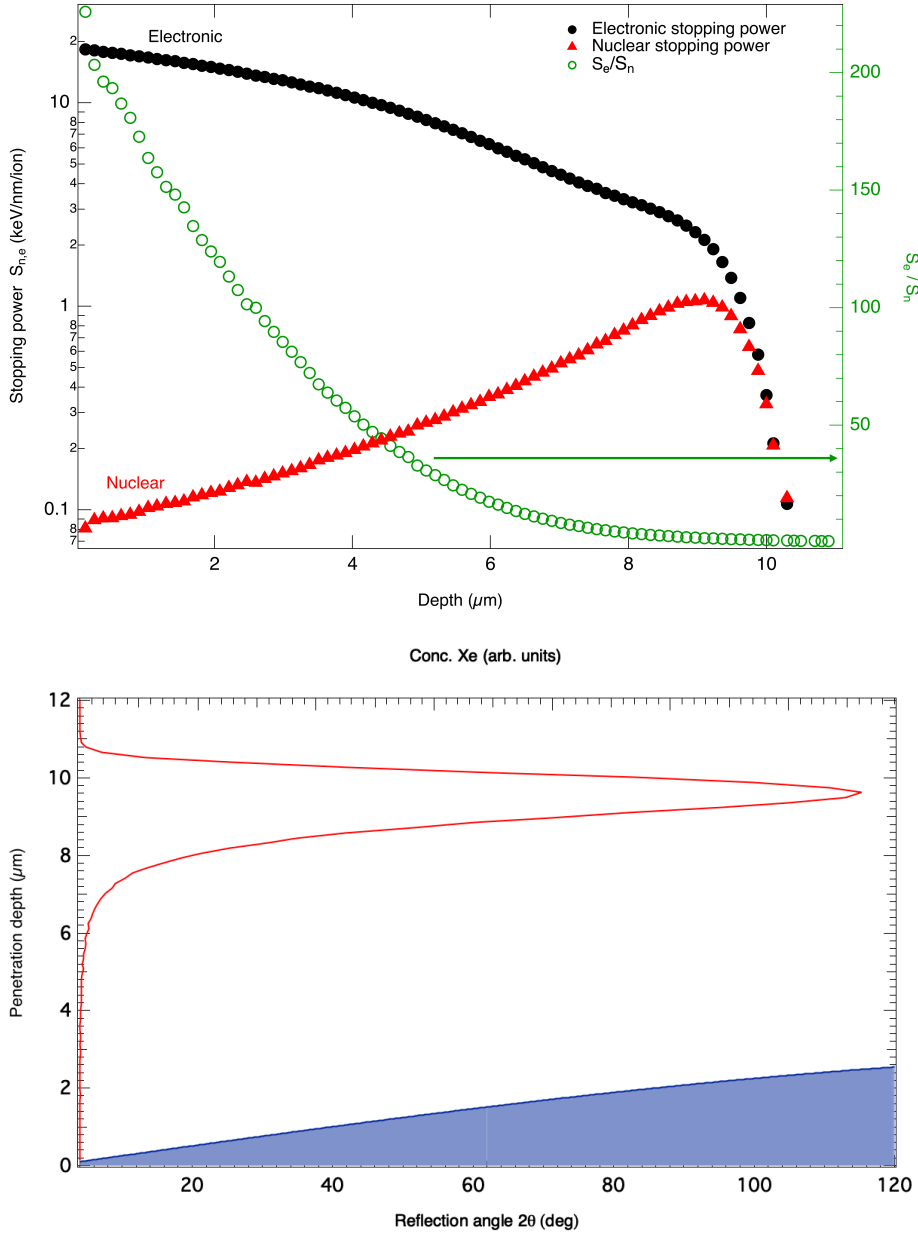


FIG. 1. (a) Electronic versus nuclear energy loss for 92 MeV Xe ions in  $\text{Gd}_2\text{Ce}_2\text{O}_7$  as a function of target depth. The ordinate on the left shows electronic (black circles) or nuclear (red triangles) energy losses on a logarithmic scale. The scale on the right shows the ratio of electronic to nuclear energy loss (green open circles). (b) Penetration depth of Cu-K $\alpha$  x-rays in  $\text{Gd}_2\text{Ce}_2\text{O}_7$  (shaded blue) for the Bragg-Brentano reflection geometry as a function of the scattering angle ( $2\theta$ , bottom scale). 97 % of the scattered intensity comes from the corresponding depth in the sample. Xe implantation profile (red line, top scale). The comparison shows all of the x-ray scattered signal comes from the irradiated region where no significant implantation occurs.

111 Electron transparent transmission electron microscopy (TEM) samples were prepared by  
112 pulverizing and crushing powder samples. Powder was equally dispersed on a holey carbon  
113 grid using high purity ethyl alcohol and subsequently observed inside a transmission electron  
114 microscope. A high tilt FEI Tecnai was operated in TEM and diffraction modes at 200 kV.  
115 For high resolution microscopy the sample was oriented preferentially utilizing selected-area  
116 electron diffraction (SAED) and calibrated CCD camera. Excitation errors were mitigated  
117 by comparing intensity symmetry relating the principal beam spot in the accompanying  
118 two-dimensional diffraction pattern. The spot electron intensity in electrons per pixel was  
119 quantitatively compared inside Digital Micrograph. The CCD camera was again normalized  
120 and stabilized over hours of continuous operation prior to observing the sample to mitigate  
121 spurious background drift and differences counting rate statistics.

### 122 III. PRISTINE $\text{Gd}_2\text{Ce}_2\text{O}_7$

#### 123 A. Symmetry analysis of the pristine phase

124 The determination of the structure of  $\text{Gd}_2\text{Ce}_2\text{O}_7$  cannot be performed using usual crys-  
125 tallographic methods because of the difficulty in growing single crystals of suitable size and  
126 perfection, a task that is made unmanageable by their complex twinning systems. There-  
127 fore, the crystallographic analysis relies on powder diffraction methods and upon transmis-  
128 sion electron microscopy that is effective for examining thin single crystal regions that are  
129 typically untwinned and therefore highly suitable for the analysis of systematic extinctions  
130 and symmetry element determination.

131 The X-ray powder diffraction pattern of pristine  $\text{Gd}_2\text{Ce}_2\text{O}_7$  (Fig. 2) can be successfully  
132 indexed using a crystal structure akin to the bixbyite C-type  $\text{Gd}_2\text{O}_3$ , though the O sto-  
133 ichiometry of the current compound requires filling half of the vacancies of the bixbyite  
134 structure. If the vacancy sub-lattice is half-filled at random, then the space group of the  
135 long-range structure of this compound is  $\text{Ia}\bar{3}$  as for the ideal bixbyite [29, 30]. On the other  
136 hand, if the vacancy distribution is not random in the vacancy sub-lattice, then the sym-  
137 metry of the system will be described by a subgroup of this disordered parent structure.  
138 To assess this point, we have used TEM to closely inspect the extinction rules of SAED  
139 patterns obtained for selected zone axes.

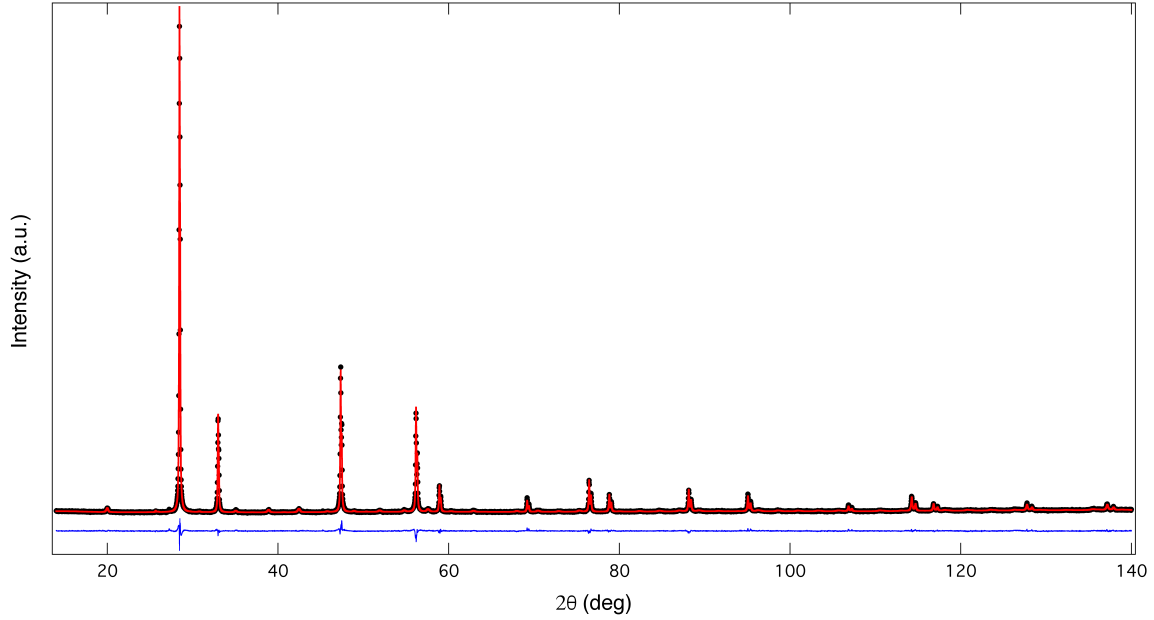


FIG. 2. Observed (black dots), calculated (red solid line) XRD pattern for pristine  $\text{Gd}_2\text{Ce}_2\text{O}_7$  showing the Rietveld fit with a disordered anion-excess bixbyite model ( $I2_13$ ,  $a=10.8515(1)$  Å,  $Z=32$ ). The blue solid line indicates the difference between the observed and calculated patterns.

140 Fig.3 displays the  $[111]$  zone axis of the reciprocal lattice of a bixbyite structure (the  
 141 lattice parameter of this cubic structure is twice the one of the corresponding fluorite). In  
 142 this picture, the reflections of type  $\{1\bar{1}0\}$  forming the hexagonal asterism centred at the  
 143 reciprocal lattice center are clearly observed, though they are in principle forbidden by the  
 144  $a$ -glide of the bixbyite space group. Therefore, a subgroup of  $Ia\bar{3}$  without glide-mirror must  
 145 be considered. The most symmetric subgroup compatible with this requirement is  $I2_13$ . The  
 146 lost symmetry operation can be used to generate the required coset of independent atoms for  
 147 this structural model. The trial structural model is summarized in Table I. In this model,  
 148 there are three independent cation sites and 4 independent anion sites.

149 The ideal bixbyite vacant sites are represented by the atomic sites  $O_{\square}$  and  $O_1$  in this  
 150 space group. Choosing different occupancies for these two sites breaks the glide mirror.  
 151 Therefore, the simplest model that puts intensities on the  $\{1\bar{1}0\}$  diffraction spots can be  
 152 obtained by localising all the "extra" O atoms of this compound at either of the two sites.  
 153 The simulated the electron diffraction pattern were generated using SingleCrystal<sup>TM</sup> [31]  
 154 assuming the O vacancies localized at  $O_{\square}$  position produces the desired effect represented  
 155 in Fig. 3.



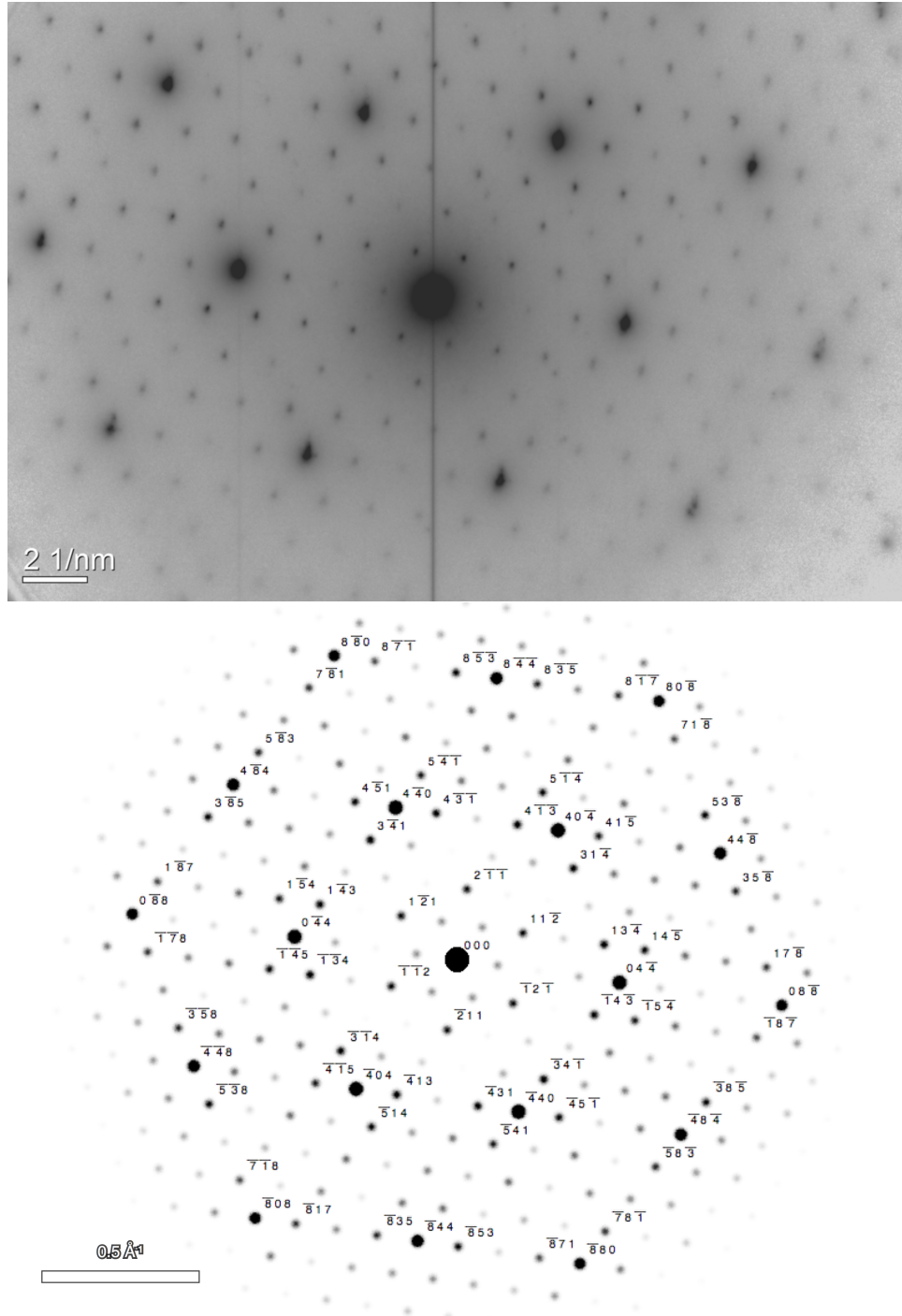


FIG. 3. Top panel: Electron diffraction pattern corresponding to the  $[111]$  zone axis in pristine  $\text{Gd}_2\text{Ce}_2\text{O}_7$ . Bottom panel: Simulated electron diffraction pattern using the initial structural model of Table I corresponding to the same  $[111]$  zone axis.

TABLE I. Initial structural model for the anion-excess bixbyite model in the  $I2_13$  space group with  $a \approx 10.85 \text{ \AA}$ ,  $Z=32$ ). The values of  $\beta$ ,  $\gamma$  and  $\delta$  are about  $10^{-2}$ .

Atom	Site	x/a	y/a	z/a	occupancy
M <sub>1</sub>	12b	$-\beta$	0	1/4	1
M <sub>2</sub>	12b	$\beta$	0	3/4	1
M <sub>3</sub>	8a	1/4	1/4	1/4	1
O <sub>□</sub>	8a	7/8	7/8	7/8	0
O <sub>1</sub>	8a	$1/8 + \gamma$	$1/8 + \gamma$	$1/8 + \gamma$	1
O <sub>2</sub>	24c	$3/8 + \delta_1$	$1/8 + \delta_2$	$3/8 + \delta_3$	1
O <sub>3</sub>	24c	$5/8 - \delta_1$	$7/8 - \delta_2$	$5/8 - \delta_3$	1

## 156 B. Modelling of the X-ray scattered intensities

157 During an X-ray scattering experiment, the plane-wave impinging beam scatters off the  
 158 sample, with the emitted radiation proportional to the Fourier transform of the charge den-  
 159 sity in the sample. The intensity of the scattered beam is then given by the Fourier transform  
 160 of the equal-time electron density-density correlation function. Diffuse scattering is due to  
 161 deviations in space and/or time from an average structure that has strict long-range order  
 162 characteristics. Periodic compositional modulations, twins, domains, or, more generally,  
 163 coherent internal interfaces, that are characteristic of lamellar or shear-type structures [33–  
 164 36] can mutually interact leading to complex short-range arrangements that can alter the  
 165 diffracted intensities.

166 As long as an average structure of a disordered crystal can be defined, the scattering  
 167 intensity can be divided into two additive contributions. The first one comes from the  
 168 strictly long-range average structure, which is periodic in space and that produces the usual  
 169 "Bragg" scattering. The second one describes the fluctuations in space (and time) around  
 170 the strict long-range order average structure: this contribution is characterized by shorter  
 171 range correlations and it is responsible for the observed diffuse scattering. Neder et al  
 172 [32] have developed a general method for describing quantitatively the diffuse scattering by  
 173 correlated microdomains.

174 In pristine  $\text{Gd}_2\text{Ce}_2\text{O}_7$ , distinct broadening rules affect the reflections characteristic of  
 175 the bixbyite superstructure of a given microdomain, where the vacancies order according

176 to a pattern, and the reflections characteristic of the fluorite average structure. Therefore,  
 177 they require the specific modelling of the diffuse scattering produced by the characteristic  
 178 order of the O vacancies in their respective correlated microdomains [37]. The information  
 179 about the short-range order is drawn from the average structure before analysing diffuse  
 180 scattering contributions because the intensities of fluorite Bragg peaks at lattice vectors  $\mathbf{G}$   
 181 are still predominant. Since fractional occupancies for the anion sub-lattice are expected,  
 182 the occupancy modulation and the displacive disorder close to these sites are possibly in-  
 183 volved in the production of diffuse scattering at the reciprocal lattice positions  $\mathbf{G}+\mathbf{q}$  of the  
 184 bixbyite structure, where  $\mathbf{q}$  is the reciprocal space vector defining the position of the diffuse  
 185 scattering signal outside of the fluorite reflections located at  $\mathbf{G}$ . The starting model for the  
 186 refinement uses the structure of Table I. The deviation from the perfect crystalline order  
 187 springs either from atomic displacement or from atomic substitutions or from a combination  
 188 of these two effects. The disorder detected in X-ray diffuse scattering experiments can be  
 189 either dynamic (related to lattice vibrations) or static (displacive, arising from substitutions  
 190 and crystalline imperfections). In conventional laboratory measurements (and in these ex-  
 191 periments in particular), the diffracted beam is measured without energy resolution, and it  
 192 cannot discriminate between the two aforementioned possibilities. The scattered intensity  
 193 then gives directly access to instantaneous spatial correlations [38, 39] of the order param-  
 194 eter  $\eta$ :  $S(\mathbf{q}, t = 0) = |\eta_{\mathbf{q}}|^2$ . Here  $\eta_{\mathbf{q}}$  is the  $q$ -th component of the Fourier transform of the  
 195 spatially-dependent modulation wave describing the O vacancy occupancy and the related  
 196 atomic displacements. The refined structural parameters of this model are summarized in  
 197 Table II.

### 198 C. Structural characteristics of the pristine phase

199 Table III summarises the structural motif of  $\text{Gd}_2\text{Ce}_2\text{O}_7$ , which consists of three different  
 200 polyhedra. The one centred around  $M_1$  is a distorted cube, the one of  $M_2$  a distorted  
 201 octahedron and the one of  $M_3$  a 7-fold coordinated capped octahedron. These polyhedra are  
 202 stacked into slabs normal to the threefold axis and they repeat indefinitely. In each slab,  
 203 there are 4 vacancies: one of them is in a cage surrounded by three corner-sharing octahedra,  
 204 the three other ones are in cages formed by two octahedra and a capped octahedron also  
 205 sharing corners (see Fig. 4). The remainder of the slab contains distorted cubes that share

TABLE II. Structural parameters of the refined anion-excess bixbyite model ( $I2_13$ ,  $a=10.8515(1)$  Å,  $Z=32$ ). The refinement converges to a  $R_{wp}=2.0\%$  and  $R_B=5.96\%$ . The refined microdomain size is  $34(2)$  nm. A common isotropic thermal displacement parameter (B) was employed for all atoms.

Atom Site	x/a	y/a	z/a	occupancy	B(Å <sup>2</sup> )
M <sub>1</sub>	12b -0.0124(13)	0	1/4	1	0.36(12)
M <sub>2</sub>	12b 0.0095(14)	0	3/4	1	0.36(12)
M <sub>3</sub>	8a 1/4	1/4	1/4	1	0.36(12)
O <sub>□</sub>	8a 7/8	7/8	7/8	0	
O <sub>1</sub>	8a 0.099(4)	0.099(4)	0.099(4)	1	0.36(12)
O <sub>2</sub>	24c 0.395(4)	0.149(5)	0.392(4)	1	0.36(12)
O <sub>3</sub>	24c 0.616(4)	0.872(4)	0.632(5)	1	0.36(12)

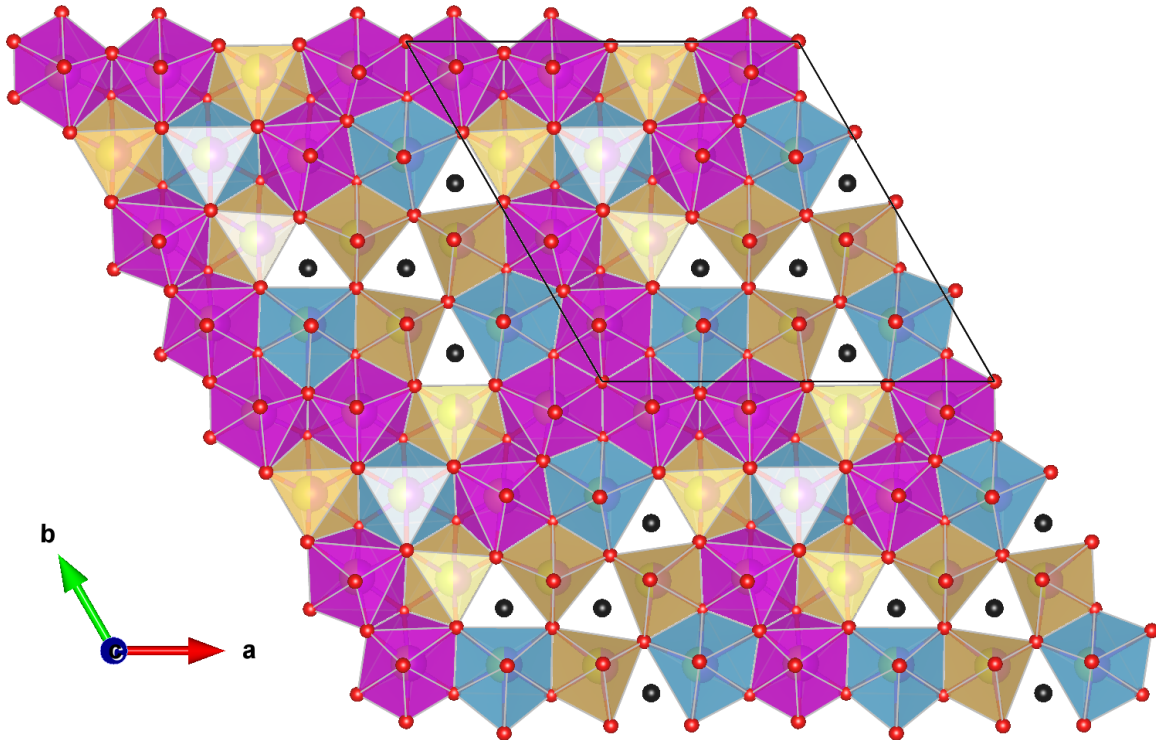


FIG. 4. Polyhedral model of a slab of pristine  $Gd_2Ce_2O_7$  obtained by the Rietveld refinement (Table III). Four reference cells are displayed. Gold is the octahedron, purple the distorted cube and blue is the capped octahedron. Black spheres materialize the O vacancies.

TABLE III. Bond lengths ( $\text{\AA}$ ) in the three polyhedra of the refined anion-excess bixbyite model.

	cube		octahedron		capped octahedron	
$M_1-O_3$	2.20(5)	$M_2-O_2$	2.03(5)	$M_3-O_{\square}$	2.35	
$M_1-O_3$	2.20(5)	$M_2-O_2$	2.03(5)	$M_3-O_3$	2.35(5)	
$M_1-O_1$	2.30(5)	$M_2-O_{\square}$	2.41(1)	$M_3-O_3$	2.35(5)	
$M_1-O_1$	2.30(5)	$M_2-O_{\square}$	2.41(1)	$M_3-O_3$	2.35(5)	
$M_1-O_3$	2.41(5)	$M_2-O_3$	2.41(5)	$M_3-O_2$	2.46(5)	
$M_1-O_3$	2.41(5)	$M_2-O_3$	2.41(5)	$M_3-O_2$	2.46(5)	
$M_1-O_2$	2.46(5)	$M_2-O_2$	2.46(5)	$M_3-O_2$	2.46(5)	
$M_1-O_2$	2.46(5)	$M_2-O_2$	2.46(5)	$M_3-O_1$	2.84(5)	
$\langle M_1 - O \rangle$	2.34	$\langle M_2 - O \rangle$	2.30	$\langle M_3 - O \rangle$	2.47	
Volume ( $\text{\AA}^3$ )	21.30		13.81		20.59	

edges with themselves and the two other polyhedra.

This represents a significant difference in the structural motif when compared to pyrochlore structures where only distorted cubes and octahedra are encountered [40]. On the other hand, this variety of polyhedra is characteristic of weberite-type  $\text{Ln}_3\text{MO}_7$  structures, though they do not share the same connectivities.

The spatial correlation length of the  $q$ -th component of the order parameter can be obtained from the breadth of the diffuse scattering within the Ornstein-Zernike formalism [41, 42]. To this purpose, a Scherrer-type peak broadening was included in the correlated Rietveld model [43] providing the characteristic long-range correlation length of the microdomains in real space. Eventually, a microstrain-type peak broadening [44, 45] can also be introduced to account for defect-induced elastic fluctuations of the lattice parameter. The measured size of the microdomains of oxygen-excess bixbyite is 34(2) nm. On the other hand, the correlation length of the average structure is 116(2) nm.

#### IV. RADIATION EFFECTS IN $\text{Gd}_2\text{Ce}_2\text{O}_7$

Figure 5 shows the changes occurring in the X-ray powder diffraction patterns of the pristine and from the damaged layer of the samples irradiated at several fluences. Rietveld refine-

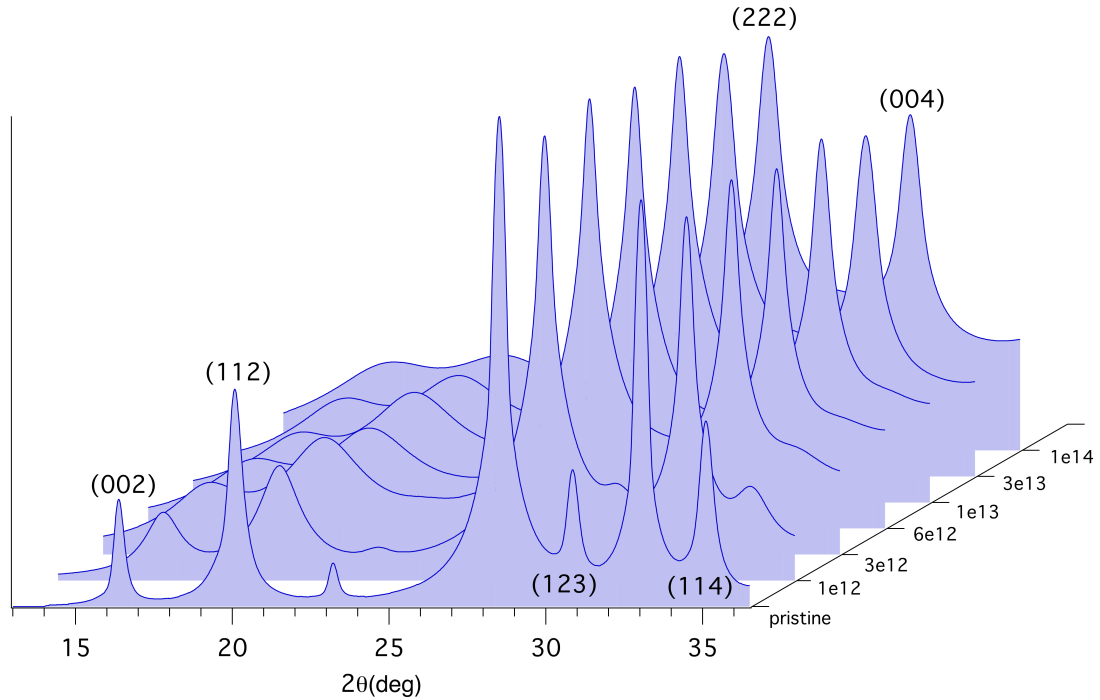


FIG. 5. Detail of the XRD patterns obtained from pristine and irradiated  $Gd_2Ce_2O_7$  as a function of increasing fluence. The intensities are represented using a logarithmic scale to display the noticeable broadening of the peaks carrying the information about the periodic stacking of O vacancies in the anion-excess bixbyite structure. These sensitive reflections are those that do not fold onto the reflections of an F-centred cubic lattice with halved parameters.

222 ments of the correlated microdomains in the irradiated samples were performed proceeding  
 223 with the same model described for the pristine samples. The characteristic broadening of  
 224 the two families of reflections still provides the measure of the separate correlation lengths  
 225 describing the anion sub-lattice (microdomain size) and the cation sub-lattice (length scale  
 226 describing the periodic arrangement of the average cation). The refinements also provide a  
 227 measure of the lattice strain and of its variance (microstrain) as a function of the irradiation  
 228 fluence. Upon irradiation, the peaks characteristic of the oxygen-excess bixbyite reflections  
 229 display an accelerated broadening and the diffuse signal almost fades out at the highest  
 230 fluence (Fig. 5). On the other hand, the broadening of the reflections characteristic of the  
 231 average cation periodicity is milder: the crystal periodicity of the cation sub-lattice is only  
 232 marginally affected and there is no clear evidence of any forthcoming amorphisation.

233 Fig. 6 (top panel) and 6 (middle panel) display the quantitative changes in the char-  
234 acteristic correlation lengths of the two sub-lattices of  $\text{Gd}_2\text{Ce}_2\text{O}_7$ . These two correlation  
235 lengths contains information about how much the ordered arrangements in each one of the  
236 two sub-lattices influence their distant neighbors.

237 The disorder quenching effect on the anion sub-lattice is extremely pronounced: the  
238 characteristic correlation length describing the vacancy distribution promptly drops from  
239 34 nm to about 5 nm (Fig 6) immediately after the lowest irradiation fluence. Increasing  
240 the fluence, this correlation length slowly relaxes to an asymptotic value of about 2 nm.  
241 The effect of radiation damage seems to bring the anion sub-lattice system very far from  
242 the equilibrium conditions straight away as soon as the ion irradiation of the sample starts.

243 The effect on the cation sub-lattice is also very pronounced in the quenched systems  
244 immediately after the lowest irradiation fluence, but it seems to saturate very quickly to a  
245 larger asymptotic value, closer to 30 nm (Fig. 6). This suggests that the absence of any  
246 appreciable site selectivity for the cations prevents the glassy behaviour observed for the  
247 anion sub-lattice.

248 In order to quantify and understand the mechanistic consequences of the radiation in-  
249 duced defects, changes in the strain and micro-strain as a function of fluence are shown in  
250 Figure 6 (bottom panel). It can be seen that, after a relatively modest increase of the lattice  
251 strain after irradiation at the lowest fluence, the strain is reduced at higher fluences while the  
252 strain variance increases. This result is in relative good agreement with an increased density  
253 of topological defects as the irradiation progresses. This is mainly related to the fact that  
254 the high density of microdomain walls acts as a sink for accommodating the point defects  
255 created during radiation, thus reducing the measured macroscopic strain but increasing its  
256 variance.

## 257 V. DISCUSSION

258 Without cation selectivity, the mixed oxides of the rare earths can be related to the  
259 binary compound series  $\text{M}_n\text{O}_{2n-2}$  where  $n$  is an integer  $\geq 4$ , famously known as Eyring's  
260 homologous series. In these series, typically observed for the Ce, Pr, and Tb oxide systems,  
261 the crystal structures corresponding to  $n= 4, 7, 9, 10, 11,$  and  $12$  are well established. These  
262 phases are fluorite-related and their symmetries are dictated by the particular way the O

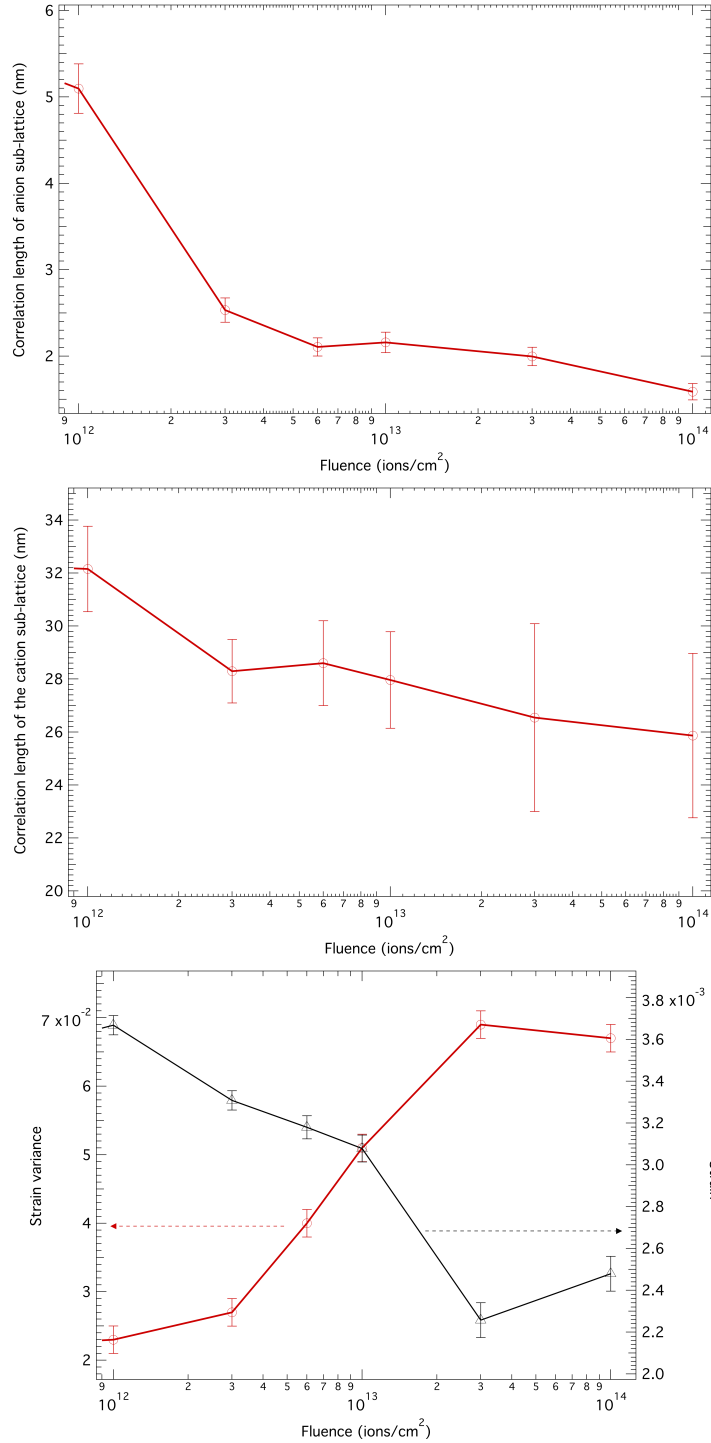


FIG. 6. Top panel: Correlation length of the anion sub-lattice as a function of fluence in  $\text{Gd}_2\text{Ce}_2\text{O}_7$ . This correlation length in pristine samples is about 34 nm. Middle panel: Correlation length of cation sub-lattice as a function of fluence in  $\text{Gd}_2\text{Ce}_2\text{O}_7$ . This correlation length in pristine is about 116 nm. Bottom panel: Strain and strain variance obtained from Rietveld analysis as a function of the Xe ion fluence. The strain and its variance are near zero for the pristine sample.



263 vacancies order [12]. The problem is generally more complex in ternary compounds when  
264 the cations also order and generally compete with the O vacancy distribution but, in the  
265 current case, the ionic radius difference and the vanishing cation mismatch (variance) do  
266 not favor any significant cation order. The symmetry of these systems is then mainly ruled  
267 by the distribution of O vacancies. This characteristic feature seems to be the hallmark of  
268  $\text{Gd}_2\text{Ce}_2\text{O}_7$ . Nevertheless, the particular oxygen stoichiometry of the current system is not  
269 among the the crystal structures found for the binary systems (Eyring's series) but it is at an  
270 intermediate position between the trigonal  $\zeta\text{-Pr}_9\text{O}_{16}$  ( $n = 9$ ) and the trigonal  $\iota\text{-Pr}_7\text{O}_{12}$ -type  
271 structure ( $n = 7$ ). These two phases only differ by the spacing of their respective planar  
272 defect features, an effect that typically leads to the intergrowth of layers of variable thickness  
273 with topotaxial relationships between these two phases in a way similar to stacking faults.

274 The oxygen-excess bixbyite  $\text{Gd}_2\text{Ce}_2\text{O}_7$  requires filling up half of the vacant sites in the C-  
275 type bixbyite structure. This unexpected result suggests the vacancy stacking according to  
276 a bixbyite-like rule is preferred to the slightly different vacancy stacking of the trigonal  $\zeta$  and  
277  $\iota$  phases that have stoichiometries framing the one of the current compound. The apparent  
278 attraction for the bixbyite stacking was already discussed in the study of the irradiation  
279 behaviour of the system  $\delta\text{-Sc}_4\text{Hf}_3\text{O}_{12}$  where cations do not display any marked long-range  
280 order [43].

281 The fact that pristine  $\text{Gd}_2\text{Ce}_2\text{O}_7$  is a wide-gap semiconductor means that boundaries  
282 among these correlated microdomains and their dynamics cannot be treated as perfect insu-  
283 lators [33]. In particular, the fact that domain walls can be charged or uncharged, straight  
284 or curved, makes the assumption of equilibrium structures simply not likely. Depletion and  
285 accumulation of O vacancies can occur at or near interfaces and domain walls. Charges  
286 can accumulate or leak off with various relaxation times, and these and other causes can  
287 produce long-lived out-of-equilibrium structures, because the relaxation mechanism can be  
288 kinetically inhibited, eventually leading to states that can have some characteristics of a  
289 domain glass.

290 The reduction of correlation length induced by the ion irradiation can be understood by an  
291 analogy with a temperature transformation. During irradiation, the crystalline system un-  
292 dergoes a phase transition from a large collection of ordered microdomains all characterised  
293 by an oxygen-excess bixbyite structure to a disordered fluorite structure where cation and  
294 anion sites are statistically occupied according to their particular stoichiometries. Once

295 the perturbation produced by irradiation is switched off, the single homogeneous disordered  
296 phase is suddenly quenched to a broken-symmetry phase where domains of the equilibrium  
297 bixbyite phase form and coarsen with time as the system achieves local equilibrium on larger  
298 and larger scales. The result of the irradiation experiment suggests that this process of re-  
299 turn to equilibrium has two very different length-scales for each one of the two sub-lattices  
300 of the crystal.

301 Since the two cations do not display any prominent tendency to order, their statistical  
302 mixing produced by the irradiation lets them almost freely rearrange over relative large  
303 length-scales. The moot concept of the theoretical Kauzmann temperature [46], if it exists  
304 for these systems, could be useful to describe this transformation with the analogy with a  
305 supercooled liquid pattern of O vacancies and their corresponding crystalline state. In the  
306 present context, the Kauzmann temperature can loosely describe the temperature at which  
307 O vacancy patterns freeze-in. This frustrated vacancy arrangement is then responsible for  
308 the shorter length-scale characterizing the anion sub-lattice and for the appearance of the  
309 topological defects separating the regions characterized by a different orientational order of  
310 the oxygen-excess bixbyite phase.

311 The increase of the strain variance can be loosely interpreted as the transition from a  
312 system characterized by an auxiliary field which varies smoothly in space to a system with  
313 a defined order parameter in each of the oxygen-excess bixbyite microdomains (this order  
314 parameter has a constant value everywhere except in correspondence with the microdomain  
315 walls). This describes a situation where the frustrated local order is not strong enough  
316 to impose its orientational symmetry long-range, and therefore, it exists in a long-range  
317 structure that is all the same characterized by cations that live in a periodic space.

318 The study of pristine and irradiated  $\text{Gd}_2\text{Ce}_2\text{O}_7$  provides a complex picture of a system  
319 that retains a considerable periodic order even at high irradiation fluences. Under severe  
320 irradiation, the correlation length of the anion sub-lattice saturates to a very small value of  
321 few nanometers. What are the consequences of this small correlation length characterizing  
322 the anion sub-lattice on the energy dissipation in the material during the irradiation? The  
323 fluctuation-dissipation theorem [47, 48] establishes a relation between equilibrium correlation  
324 functions and linear response functions. Perhaps we can establish a moot analogy between  
325 this behavior and what happens in a turbulent flow [49]. Physically, energy is dissipated  
326 because of the work done by the fluctuating viscous stresses in resisting deformation of the

327 fluid material by the fluctuating strain rates. When turbulence is present, it usually domi-  
 328 nates all other flow phenomena and it results in increased energy dissipation, mixing, heat  
 329 transfer, and drag. The dissipation of turbulence energy mostly takes place at the smallest  
 330 turbulence scales, and that those scales can be characterized by the so-called Kolmogorov  
 331 microscale defined by:  $\eta_K = \left(\frac{\nu^3}{\varepsilon}\right)^{1/4}$  where  $\varepsilon$  is the average rate of dissipation of turbulence  
 332 kinetic energy per unit mass, and  $\nu$  is the kinematic viscosity of the fluid. In atmospheric  
 333 motions, typical values of the Kolmogorov microscale range from 0.1 to 10 millimeters. In  
 334 laboratory flows, where the overall scale of the flow is greatly reduced, much smaller values  
 335 of  $\eta_K$  are not uncommon. Viscous scales (operating on a time scale of  $t_K = \left(\frac{\nu}{\varepsilon}\right)^{1/2}$  dissipate  
 336 rapidly any energy sent down to them by the non-linear processes of scale to scale energy  
 337 transfer. The coarse-grained approach for the spatial averaging of the cation sub-lattice  
 338 seems then an effective way for introducing field fluctuations and dissipation described by  
 339 the correlation length of the anion sub-lattice. The very short correlation length describing  
 340 the spatial distributions of the topological defects in this system where otherwise the crys-  
 341 tallinity continues to be described by a significantly longer characteristic correlation length,  
 342 can explain why the non-equilibrium dynamics of this open system is so effective in dissi-  
 343 pating the energy of the irradiation process, allowing the system to remain crystalline at  
 344 fluences where many other fluorite-related counterpart systems amorphise. To some extent,  
 345  $\text{Gd}_2\text{Ce}_2\text{O}_7$  behaves like a functional material because its topological defects effectively lead  
 346 to very strong enhancements of the radiation resistance properties. Microdomain walls cre-  
 347 ate localized sinks that can efficiently absorb part of the defects concentrations generated  
 348 by irradiation but also effectively dissipate the energy in the Kolmogorov's picture [49] re-  
 349 taining much of the long-range periodic properties of the cation sub-lattice of the pristine  
 350 structure.

351 This highly effective radiation response of this material might be universal to the class of  
 352 oxygen deficient fluorites displaying a distinctive O vacancy ordering in the anion sub-lattice  
 353 without any particular cation ordering, providing the decoupling of the order characteristics  
 354 of the two sub-lattices and opening the way for a coarse-grained approach to this system. The  
 355 existence of mobile antiphase boundaries within a coarse-grained periodic system seems to  
 356 provide an extremely effective pathway to dissipate the energy introduced by the irradiation  
 357 process, thus avoiding the amorphisation of the crystal structure that is typically observed  
 358 in fluorite-related systems where the cations are ordered.

359 **ACKNOWLEDGMENTS**

360 The authors would like to acknowledge Dr. Isabelle Monnet and Dr. Jean-Claude Pivin  
361 for their help in performing the ion irradiation experiment at GANIL.

---

- 362 [1] O. T. Sørensen, *Nonstoichiometric Oxides* 1st Edition, Academic Press, 1981
- 363 [2] D. J. M. Bevan, W. W. Barker, R. L. Martin, and T. C. Parks, Mixed oxides of the type  $\text{MO}_2$   
364 (fluorite  $-\text{M}_2\text{O}_3$ . Part 2: Non stoichiometry in ternary rare-earth oxide systems. *Proceedings*  
365 *of the Fourth Conference on Rare Earth Research*, 441-468 (1964).
- 366 [3] J. O. Sawyer, B. G. Hyde, and L. Eyring. Fluorite-related homologous series in the rare earth  
367 oxides. *Bull. Soc. Chim. France*, 1190 (1965).
- 368 [4] B. G. Hyde, D. J. M. Bevan, and L. Eyring, *Phil. Trans.*, **259A**, 583 (1966).
- 369 [5] G. Brauer. Structural and solid state chemistry of pure rare earth oxides and hydroxides in  
370 *Progress in the Science and Technology of the Rare Earths*. vol 3. 434–458. Pergamon, (1966).
- 371 [6] D. J. M. Bevan and E. Summerville, Mixed rare earth oxides Chapter **28** 401–524 in *Handbook*  
372 *on the Physics and Chemistry of Rare Earths*, Ed. K. A. Gschneidner, Jr. and L. Eyring  
373 Volume **3**. North-Holland Company (1979).
- 374 [7] J. D. McCullough, and J. D. Britton. X-ray studies of rare earth oxide systems II. *J. Am.*  
375 *Ceram. Soc.*, **74** 5225-5227 (1952).
- 376 [8] I. F. Ferguson, and P. G. T. Fogg, The oxides of uranium. Part VIII. The system uranium  
377 dioxide-yttria. *J. Chem. Soc.*, 3679-3681 (1957).
- 378 [9] G. Brauer, and H. Gradinger. Über heterotype Mischphasen bei Seltenerdoxyden. I. *Z. anorg.*  
379 *allg. Chem.* **276** 209-226 (1954).
- 380 [10] G. Brauer, and H Gradinger. Über heterotype Mischphasen bei Seltenerdoxyden. II. Die  
381 Oxydsysteme des Cers und des Praseodyms. *Z. anorg. allg. Chem.*, **277**, 89-95 (1954).
- 382 [11] G. Brauer, and U. Holtschmidt. Über die Oxyde des Cers. III. *Z. anorg. allg. Chem.*, **279**  
383 129-137 (1955).
- 384 [12] P. Kunzmann, L. J. Eyring. On the crystal structures of the fluorite-related intermediate  
385 rare-earth oxides. *Solid State Chem.*, **14**, 229-237 (1975).
- 386 [13] Z. C. Kang Lanthanide higher oxides: the contribution of Leroy Eyring. Chapter **236** in

- 387 *Handbook on the Physics and Chemistry of Rare Earths*, Volume **38**. Elsevier (2008).
- 388 [14] Y. Ikuma, S. Anandan, and K. Niwa, Lattice parameter, defect concentration and oxygen  
389 diffusion in ceria solid solutions, *Transactions of the Materials Research Society of Japan*, **35**  
390 485-489 (2010)
- 391 [15] D. L. Drey, E.C. O’Quinn, T. Subramani, K. Lilova, G. Baldinozzi, I. M. Gussev, A. F.  
392 Fuentes, J. C. Neuefeind, M. Everett, D. Sprouster, A.Navrotsky, R. C. Ewing, M. Lang,  
393 Disorder in  $\text{Ho}_2\text{Ti}_{2-x}\text{Zr}_x\text{O}_7$ : pyrochlore to defect fluorite solid solution series. *RSC Advances*,  
394 **10**, 34632–34650 (2020).
- 395 [16] K. Wurst, E. Schweda, D.J.M Bevan, J Mohyla, K.S Wallwork, M Hofmann, Single-crystal  
396 structure determination of  $\text{Zr}_{50}\text{Sc}_{12}\text{O}_{118}$ , *Solid State Sciences*, **5**, 1491–1497 (2003).
- 397 [17] S. Meyer, E. Schweda, M. N. J. Martinez, H. Boysen, M. Hoelzel, T. Bredow, Neutron pow-  
398 der diffraction study and DFT calculations on the structure of  $\text{Zr}_{10}\text{Sc}_4\text{O}_{26}$ , *Zeitschrift für*  
399 *Kristallographie*, **224** 539–543 (2009).
- 400 [18] M. R. Thornber, D. J. M. Bevan, and J. Graham. Mixed oxides of the type  $\text{MO}_2(\text{fluorite})$ -  
401  $\text{M}_2\text{O}_3$ . III. Crystal structures of the intermediate phases  $\text{Zr}_5\text{Sc}_2\text{O}_{13}$  and  $\text{Zr}_3\text{Sc}_4\text{O}_{12}$ . *Acta Cryst.*  
402 *B*, **24** 1183–1190 (1968).
- 403 [19] M. Lang, et al., Review of  $\text{A}_2\text{B}_2\text{O}_7$  pyrochlore response to irradiation and pressure. *Nuclear*  
404 *Instruments and Methods in Physics Research Section B: Beam Interactions with Materials*  
405 *and Atoms*, **268** 2951–2959 (2010).
- 406 [20] Y. H. Li, B. P. Uberuaga, C. Jiang, S. Choudhury, J. A. Valdez, M. K. Patel, J. Won, Y.-Q.  
407 Wang, M. Tang, D. J. Safarik, D. D. Byler, K. J. McClellan, I. O. Usov, T. Hartmann, G.  
408 Baldinozzi, and K. E. Sickafus *Phys. Rev. Lett.*, **108**, 195504 (2012).
- 409 [21] J. Shamblin, M. Feygenson, J. Neuefeind, C. L. Tracy, F. Zhang, S. Finkeldei, D. Bosbach, H.  
410 Zhou, R. C. Ewing and M Lang, Probing disorder in isometric pyrochlore and related complex  
411 oxides *Nat. Mater.*, **15**: 507 (2016).
- 412 [22] D. Simeone, G. J. Thorogood, D. Huo, et al. Intricate disorder in defect fluorite/pyrochlore:  
413 a concord of chemistry and crystallography. *Sci. Rep.*, **7**, 3727 (2017).
- 414 [23] Pilania, G., B. Puchala, and B. Uberuaga, Distortion-stabilized ordered structures in  $\text{A}_2\text{BB}^{\prime}\text{O}_7$   
415 mixed pyrochlores. *npj Comput. Mater.*, **5**, 7 (2019).
- 416 [24] V. Grover, S. N. Achari and A. K. Tyagi *J. App. Cryst.*, **36** 1082–1084 (2003).
- 417 [25] M. K. Patel, G. Baldinozzi, J. A. Aguiar, J. A. Valdez, S. C. Vogel, and K. E. Sickafus.

- 418 Structural analysis of  $\text{Gd}_2\text{Ce}_2\text{O}_7$ . *MRS Online Proceedings Library*, **1743** 7–13 (2015).
- 419 [26] W. Feller *An Introduction to Probability Theory and its Applications*, Volume 1, 3rd edition  
420 ISBN: 978-0-471-25708-0, John Wiley and Sons (1971).
- 421 [27] J. F. Ziegler and J. P. Biersack *The Stopping and Range of Ions in Matter*, Volume **2-6**.  
422 Pergamon Press (1985).
- 423 [28] J. F. Berar and G. Baldinozzi. Xnd code : from x-ray laboratory data to incommensurately  
424 modulated phases. Rietveld modelling of complex materials. *IUCr CPD Newsletter*, **20** 3–5  
425 (1998).
- 426 [29] G. Baldinozzi, J.-F. Berar, and G. Calvarin. Rietveld Refinement of Two-Phase Zr-Doped  
427  $\text{Y}_2\text{O}_3$ . *Materials Science Forum*, **278-281**, 680–685 (1998).
- 428 [30] G. Baldinozzi, J. F. Berar, M. Gautier Soyer, and G. Calvarin. Segregation and site selectivity  
429 in Zr-doped  $\text{Y}_2\text{O}_3$ . *J. Physics-Condensed Matter*, **9**: 9731–9744 (1997).
- 430 [31] SingleCrystal<sup>TM</sup>: a single-crystal diffraction program for Mac and Windows. CrystalMaker  
431 Software Ltd, Oxford, England (www.crystallmaker.com)
- 432 [32] R. B. Neder, F. Frey and H. Schulz *Acta Cryst. A*, **46**, 792–798 (1990).
- 433 [33] R.J.D. Tilley, *Nature*, **269**, 229–231 (1977).
- 434 [34] A.M. Stoneham and P.J. Durham. The ordering of crystallographic shear planes: theory of  
435 regular arrays. *J. Phys. Chem. Solids*, **34**, 2127–2135 (1973).
- 436 [35] J. G. Allpress, and H. J. Rossell. A nanodomain description of defective fluorite-type phases  
437  $\text{Ca}_x\text{M}_{1-x}\text{O}_{2-x}$ , (M=Zr, Hf;  $x = 0.1 - 0.2$ ). *J. Solid State Chem.*, **15** 68–78 (1975).
- 438 [36] M. P. Van Dijk, F. C. Mijlhoff, and A; J. Burggraaf. Pyrochlore nanodomain formation in  
439 fluorite oxides. *J. Solid State Chem.*, **62** 377–385 (1986).
- 440 [37] M. Fevre, A. Finel, and R. Caudron. Local order and thermal conductivity in yttria-stabilized  
441 zirconia. I. Microstructural investigations using neutron diffuse scattering and atomic-scale  
442 simulations. *Phys. Rev. B*, **72**, 104117 (2005).
- 443 [38] L. Van Hove, Correlations in space and time and Born approximation scattering in systems  
444 of interacting particles. *Phys. Rev.*, **95**, 249–262 (1954).
- 445 [39] M. Kardar. Statistical physics of fields. ISBN 978-0-521-87341-3 Cambridge University Press  
446 (2007).
- 447 [40] E. C. O’Quinn, K. E. Sickafus, R. C. Ewing, G. Baldinozzi, J. C. Neufeind, M. G. Tucker,  
448 A. F. Fuentes, D. Drey, M. K. Lang. Predicting short-range order and correlated phenomena

- 449 in disordered crystalline materials. *Science Advances*, **6** eabc2758 (2020).
- 450 [41] H. Jagodzinski, and F. Frey, Disorder diffuse scattering of x-rays and neutrons, *International*  
451 *Tables for Crystallography Volume B: Reciprocal space* Ed. U Shmueli 407–442 (2006).
- 452 [42] J. Brunet, and K. E. Gubbins, General Theory of the Long Range Pair Correlation Function.  
453 *The Journal of Chemical Physics*, **49**, 5265–5269 (1968).
- 454 [43] M. K. Patel, K. E. Sickafus, and G. Baldinozzi. Divergent short- and long-range behavior in  
455 ion-irradiated  $\delta$ -Sc<sub>4</sub>Hf<sub>3</sub>O<sub>12</sub>. *Phys. Rev. Materials*, **4**, 093605 (2020).
- 456 [44] W. H. Hall. X-Ray Line Broadening in Metals. *Proc. Phys. Soc. A* **62**, 741–743 (1949).
- 457 [45] T. Ungar. Micro structural parameters from X-ray diffraction peak broadening. *Scripta Mate-*  
458 *rialia*, **51**, 777–781 (2004).
- 459 [46] W. Kauzmann, *Chem. Rev.*, **43**, 219 (1948).
- 460 [47] J. Weber, Fluctuation Dissipation Theorem, *Phys. Rev.*, **101**, 1620–1626 (1956).
- 461 [48] J. P. Hansen, F. Joly, and I. R. McDonald. Self-diffusion, interdiffusion and long wavelength  
462 plasma oscillations in binary ionic mixtures. *Physica A*, **132**, 472-488 (1985).
- 463 [49] P. Manneville *Dissipative structures and weak turbulence*. In: P. Garbaczewski, M. Wolf, A.  
464 Weron. *Chaos - The Interplay Between Stochastic and Deterministic Behaviour*. Lecture Notes  
465 in Physics, **457** (1995), Springer. doi: 10.1007/3-540-60188-0\_59.